Analyst

ROYAL SOCIETY OF CHEMISTRY

PAPER

View Article Online
View Journal | View Issue

Cite this: *Analyst*, 2021, **146**, 855

Photoelectrochemical thrombin biosensor based on perylene-3,4,9,10-tetracarboxylic acid and Au co-functionalized ZnO nanorods with signal-off quenching effect of Ag@Ag_2S†

Qiaoxia Zhang,[a] Xiangwei Liu,[a] Haoran Wang,[a] Qing Liu, *[a] Qingyun Liu *[a] and Xianxi Zhang[b]

Received 2nd November 2020,
Accepted 21st November 2020

DOI: 10.1039/d0an02167a

rsc.li/analyst

In this work, a thrombin photoelectrochemical aptasensor was reported based on a photoanode of perylene-3,4,9,10-tetracarboxylic acid (PTCA), Au nanoparticle co-functionalized ZnO nanorods (ZnO NRs) and the "signal-off" amplification effect of Ag@Ag_2S. The photocurrent response of the ZnO NRs was improved greatly due to the excellent visible-light photoelectric performance of PTCA and the surface plasmon resonance (SPR) effect of Au nanoparticles. Due to the specific recognition between thrombin and aptamers, the non-conductive complex with a steric hindrance structure blocked the diffusion path of the electron donating ascorbic acid (AA) and then the "signal-off" Ag@Ag_2S quencher was captured. The quencher blocked the irradiation light toward the ZnO NRs/PTCA/Au electrode and competitively consumed the electron donor AA that could have been involved in the oxidation reaction with photogenerated holes of PTCA, resulting in the further decrease of the photocurrent. Based on the evident photocurrent response of the photoanode and the superior quenching strategies, the detection limit of thrombin is as low as 33 fM with a wide linear detection range from 0.0001 nM to 50 nM. The prepared biosensor also exhibited good specificity, reproducibility and stability, suggesting potential application in thrombin specific detection.

Introduction

Photoelectrochemical (PEC) biosensors based on PEC sensing strategy have attracted extensive attention. Thanks to the separation of the excitation and detection signals, the PEC biosensors show advantages such as low background noise and excellent sensitivity compared to the traditional ones.[1] To a great extent, the performance of PEC biosensors depends on the property of the photosensitive electrode. So it is essential to explore functional materials with excellent and stable photoelectric properties for working electrode decoration. Among the substrate electrode materials for PEC conversion, ZnO is demonstrated as one of the most excellent candidates for PEC biosensors,[2–4] taking the inherent advantages of low cost, high thermal stability, nontoxicity, and environmental friendliness into consideration.[5] Nevertheless, the wide band gap ($E_g \approx$ 3.37 eV) of ZnO suggested its main response to light in the ultraviolet region, which is destructive for biomolecules.[4] Thus, it is important to broaden the photoresponse of ZnO in the visible region. The introduction of oxygen defects which can create defect-isolated levels in ZnO has been proved to be an effective strategy.[6–8] Moreover, the controlled synthesis of vertically aligned ZnO nanorod (ZnO NR) arrays with high electron mobility and direct electrical pathways can speed up the electron transportation, thus benefitting photocurrent generation.[4]

To further improve the initial photocurrent of the photoanode, several methods can be used to decorate the substrate material of the ZnO NRs. The decoration of organic photosensitive materials and the deposition of noble metals with surface plasmon resonance (SPR) effect are effective strategies. It is proved that the inorganic/organic nanocomposites exhibit distinctly enhanced photocurrent response. For example, an effective photosensitizer, perylene-3,4,9,10-tetracarboxylic acid (PTCA), was widely used to improve the photoelectric conversion.[9–11] PTCA can be adsorbed strongly on the surface

[a]*College of Chemical and Biological Engineering; State Key Laboratory of Mining Disaster Prevention and Control Co-founded by Shandong Province and the Ministry of Science and Technology, Shandong University of Science and Technology, Qingdao 266590, China. E-mail: qyliu@sdust.edu.cn*

[b]*Shandong Provincial Key Laboratory/Collaborative Innovation Center of Chemical Energy Storage & Novel Cell Technology; College of Chemical and Chemical Engineering, Liaocheng University, Liaocheng 252059, China*

†Electronic supplementary information (ESI) available. See DOI: 10.1039/d0an02167a

of inorganic semiconductors through the coordinate bonds between –COOH groups and ZnO, allowing electron injection from the photoactive PTCA into ZnO upon excitation by light irradiation.[12] For the plasmonic noble metal nanoparticles (such as Au, Ag, and Pt), Au NPs were the most effectively used material to enhance the photoelectric conversion in the PEC system.[13–15] Moreover, for the immobilization of aptamers, noble metals such as Pt, Au and Ag can coordinate with sulfhydryl functionalized DNA, which is in favor of the aptamer self-assembly on the surface of the electrode.[16] The Au NPs provide an immobilization platform for the sulfhydryl functionalized aptamer 1 (Apt1), which can be bonded through the Au–S bonds.

Except the improvement of the initial photocurrent, the signal amplification strategy for target detection is another important factor in the design of PEC biosensors. The "signal-off" amplification method has been widely adopted through different quenching strategies, such as steric hindrance effect,[17] precipitation,[18] light absorption competition,[19] multi-functional signal quencher[20] and so on. The adoption of sandwich-type photosensitive quenchers designed with better light absorption competition and steric hindrance effect is an effective protocol. Ag_2S is an active photosensitive semiconductor with relatively low toxicity and a narrow band gap of *ca.* 1 eV.[21] Because of its relatively small band gap, Ag_2S has an absorption in the entire visible region and near infrared (NIR) region of the solar spectrum.[22] Furthermore, sulfhydryl functionalized aptamer 2 (Apt2) can be immobilized on the surface of Ag_2S without complicated modifications.[23] For the quencher in a sandwich-type biosensor, it is vital to get well monodispersed amplifiers. However, Ag_2S nanoparticles tend to agglomerate.[24] Therefore, it is a good method to prepare Ag nanoparticles with good dispersion first, and then grow Ag_2S *in situ* on the surface of Ag. The unique inner structure of the plasmonic Ag nanoparticles can further improve the quenching effect of Ag@Ag_2S.

Herein, a novel concept of the PEC thrombin aptasensor was designed based on a photoanode of PTCA and Au nanoparticles co-functionalized ZnO NRs together with the combined "signal-off" amplification strategies. The great photocurrent of the photoanode benefited from the synergistic effect of the photosensitive ZnO NRs, PTCA, plasmonic Au nanoparticles and their staggered band structures. After specific recognition, the photocurrent signal can be decreased remarkably due to the light absorption competition of Ag@Ag_2S and the steric hindrance effect of the non-conductive biomass complex. The results confirmed the analytical performance, selectivity, reproducibility and stability of this biosensor. Moreover, this research provided a protocol for signal-off PEC sensing platforms.

Experimental section

Reagents and apparatus

The main reagents and apparatus used in this work are described in the ESI.†

Preparation of ZnO NRs

It was prepared in three steps according to the reported work[25] with modifications. The preparation details are presented in the ESI.†

Preparation of ZnO NRs/PTCA

The ITO decorated with ZnO NRs was vertically immersed in PTCA solution for about 10 min, thoroughly rinsed, and dried in the air successively. Due to the negatively charged terminal carboxylates and planar conjugated ring system of PTCA, the impregnation method is a simple and effective way to coat PTCA on the surface of ZnO.[26]

Preparation of ZnO NRs/PTCA/Au

The plasmonic Au nanoparticles were decorated on the ZnO NRs/PTCA electrodes through a facile photoreduction method. The as-prepared ZnO NRs/PTCA electrode was placed in the watch glass with the conductive side upward. A solution composed of 1 mL of aqueous solution of $HAuCl_4 \cdot 3H_2O$ (1 mg mL^{-1}) and 9 mL of absolute ethanol was added into the watch glass. The system was irradiated under 300–2500 nm light for 30 s powered by a xenon lamp (200 W).Finally, the reddish brown electrode of the ZnO NRs/PTCA/Au was synthesized successfully.

Fabrication of Ag@Ag_2S nanoparticles

The Ag@Ag_2S was prepared through two main steps. The first step is the preparation of monodispersed Ag nanoprisms strictly according to the reported method.[27] The prepared Ag nanoprisms were washed thoroughly and collected, then re-dispersed in 20 mL of H_2O. The second main step is the *in situ* growth of Ag_2S on the surface of Ag nanoprisms. About 3 mL of sodium sulphide aqueous solution (2 mM) was added to the above Ag nanoprism suspension and then the system was stirred for 20 min. Finally, the Ag@Ag_2S nanoparticles were washed, collected, and then re-dispersed in 2 mL of H_2O for further use.

Fabrication of Apt2-Ag@Ag_2S

First, 0.5 mL of Apt2 (2.0 μM) was added to the above Ag@Ag_2S suspension and the aptamer was incubated at room temperature for 1 h. The precipitate was then washed and centrifuged with PBS (pH = 7) three times. The resulting Apt2-Ag@Ag_2S was re-dispersed in 200 μL of 20 mM tris-HCl and stored at 4 °C for the following assays.

Biosensor preparation

The biosensor preparation (including the preparation of materials) is illustrated in Scheme 1. Firstly, the ITO electrode already decorated with the ZnO NRs/PTCA/Au (with a fixed working area of 1 cm × 1 cm) was covered with 20 μL of 2.0 μM Apt1 and incubated for 5 h (ZnO NRs/PTCA/Au/Apt1). Secondly, to overcome nonspecific binding, the electrode was immersed in 0.5 mM MCH for 40 min (ZnO NRs/PTCA/Au/Apt1/MCH). Thirdly, 10 μL each of TB of different concen-

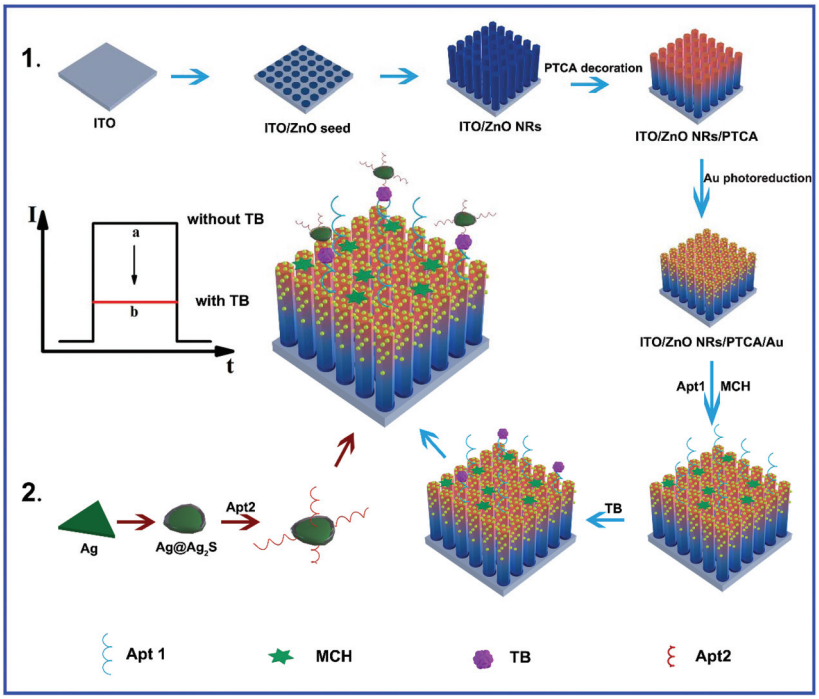

Scheme 1 Diagram of the preparation process of this biosensor.

trations was incubated on the electrode for 40 min (ZnO NRs/PTCA/Au/Apt1/MCH/TB). Finally, 20 μL of the above as-prepared Apt2-Ag@Ag_2S suspension was incubated for another 40 min (ZnO NRs/PTCA/Au/Apt1/MCH/TB/Apt2-Ag@Ag_2S). The electrode was washed with 10 mM PBS (pH 7.0) after each step and finally the electrode was stored at 4 °C for further use.

PEC assessment

The PEC assessment was carried out in 0.1 M PBS solution (pH = 7) with 0.1 M ascorbic acid (AA) by chronoamperometry measurement under intermittent visible light irradiation at a bias potential of 0 V. The irradiation light was supplied by a xenon lamp (200 W, 300–2500 nm) with a UV-cut 420 nm filter. AA was used to scavenge the photogenerated holes.

Results and discussion

Characterization of different materials

The SEM image of the ZnO NRs is depicted in Fig. 1A and the one with a higher magnification is shown in Fig. 1A. It is seen that the vertically aligned ZnO NRs with a diameter of about 69 nm grow uniformly on the surface of the ITO. The decoration of PTCA almost has no influence on the surface of the ZnO NRs (shown in Fig. S1†). After the further photoreduction of Au, many tiny nanoparticles on the surface of the ZnO NRs/PTCA/Au were found (Fig. 1B).

XRD analysis was carried out to study the compositions and crystal structure evolution after each procedure of the ZnO NRs/PTCA/Au electrode synthesis. As shown in Fig. 1C, except the diffraction peaks corresponding to the ITO substrate, all of the other peaks of ITO/ZnO NRs can be indexed to a hexagonal phase zincite (JCPDS 36-1415). Clearly, for the ITO/ZnO NRs/PTCA sample, the decoration of PTCA does not obviously affect the diffraction peaks, indicating that the PTCA almost has no impact on the crystallization of ZnO. Notably, for the ITO/ZnO/PTCA/Au sample, a new peak emerges at 2θ of *ca.* 38° after the photoreduction of Au, which is indexed to the (111) plane of Au (JCPDS 04-0784).

Fig. 1D shows the TEM image of Ag nanoprisms, which are triangular-shaped nanoplates enclosed by two (111) facets at both top and bottom surfaces.[27] After an *in situ* sulfidation treatment, as shown in Fig. 1E, the formed Ag@Ag_2S nanoparticles decrease in size and their edges become smooth compared to those of the Ag nanoprisms. Furthermore, the high resolution transmission electron microscope (HRTEM) image of Ag@Ag_2S (the region marked with red in Fig. 1E) is shown in Fig. 1F. The lattice fringes of 0.24 nm can be indexed to the (111) plane space of Ag. Moreover, on the edge of Ag@Ag_2S, there are lattice fringes of 0.28 nm, which correspond to the (−112) plane space of Ag_2S, confirming the successful preparation of Ag@Ag_2S.

To get further insights into the elemental composition and distribution of Ag@Ag_2S, the HADDF-STEM measurement (Fig. 1G) and element mapping analysis (Fig. 1H–J) were conducted and the result indicates a uniform distribution of S element on the surface of Ag, which further proves the successful preparation of the Ag@Ag_2S nanoparticles.

The chemical composition and state of the ZnO NRs/PTCA/Au electrode surface were studied through XPS analysis.

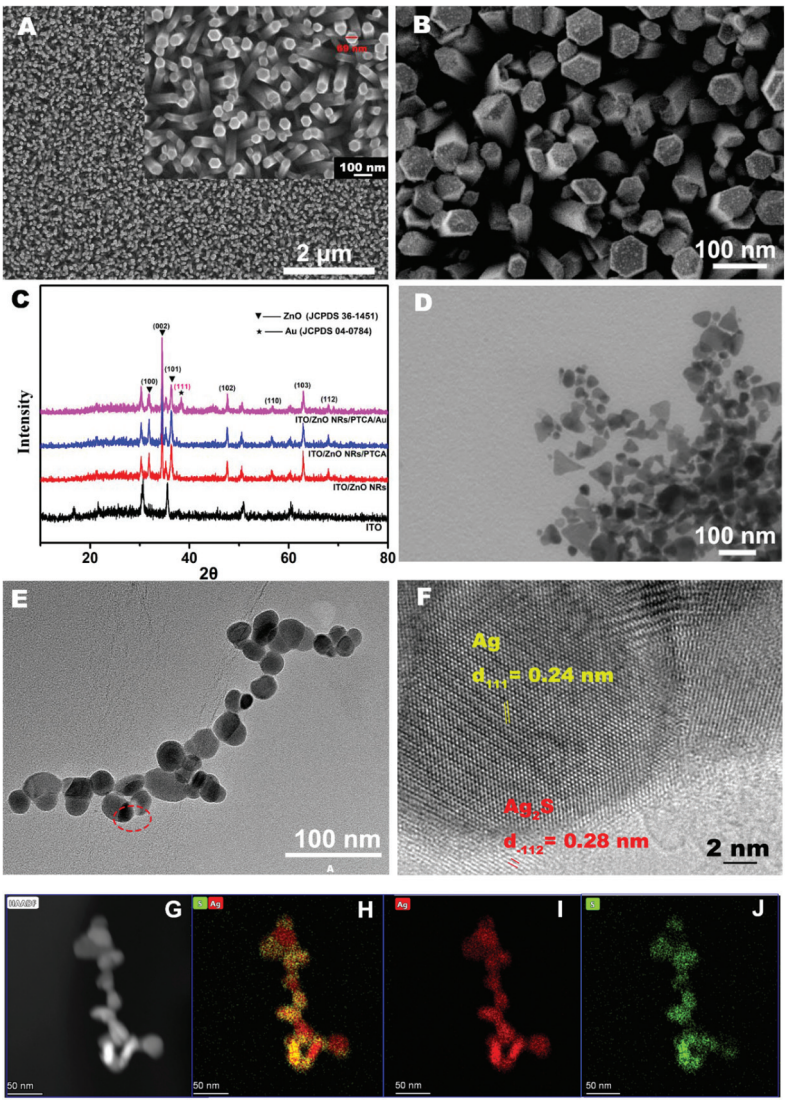

Fig. 1 SEM images of (A) ZnO NRs and (B) ZnO NRs/PTCA/Au; (C) XRD patterns of different samples; TEM images of (D) Ag and (E) Ag@Ag_2S; (F) HRTEM of Ag@Ag_2S; (G) HADDF-STEM and (H–J) EDS element mapping images of Ag@Ag_2S.

Fig. 2A shows the full survey spectrum of ZnO NRs/PTCA/Au and the expected peaks for Zn 2p, O 1s, C 1s, and Au 4f can be found. The high resolution XPS spectra for O 1s (Fig. 2B) can be resolved into two peaks located at 530.32 and 531.5, which are assigned to the Zn–O bonds and oxygen vacancies, respectively.[8,28,29] The intense peak in 531.5 is closely related to the number of oxygen vacancies within the matrix of ZnO. The oxygen defects may be due to the calcination treatment, which endowed the ZnO NRs with a photocurrent response under visible light irradiation.[29] The electrons bound by the oxygen vacancies (serving as electron donors) are easily stimulated to form free electrons to enhance the electrical conductivity of the ZnO NRs. The consumption of the photogenerated holes on the exposed high active crystal face that benefited from the oxygen vacancies can further suppress the recombination of the photogenerated electrons and holes.[30] The high resolution spectrum of C 1s in Fig. 2C can be assigned to two peaks. One peak located at 284.8 eV can be indexed to C=C/C–C of the sp^2-hybridized domains and sp^3-hybridized domains in PTCA. The other at 288.8 eV is indexed to the –COOH group of PTCA.[31,32] The result indicates that PTCA has been successfully decorated on the electrode. Finally, Fig. 2D shows the high resolution spectrum of Au 4f on the surface of the ZnO NRs/PTCA/Au electrode. The peaks at 83.4 eV and 87.2 eV belong to the 4f7/2 and 4f5/2 energy levels of Au^0, respectively, suggesting the presence of metallic state Au in the composite.[33] The peak at 91.3 eV assigned to Au^{3+} may be due to the physical absorption of $AuCl_4^-$ while the one at 89 eV indexed to Au^{2+} 4f5/2 is a transition state of Au in the reduction process.[34] According to the results discussed above, it can be concluded that Au has been decorated on the working electrode successfully.

The UV-vis diffuse reflection spectra of the ZnO NRs, ZnO NRs/PTCA and ZnO NRs/PTCA/Au electrodes are used to study

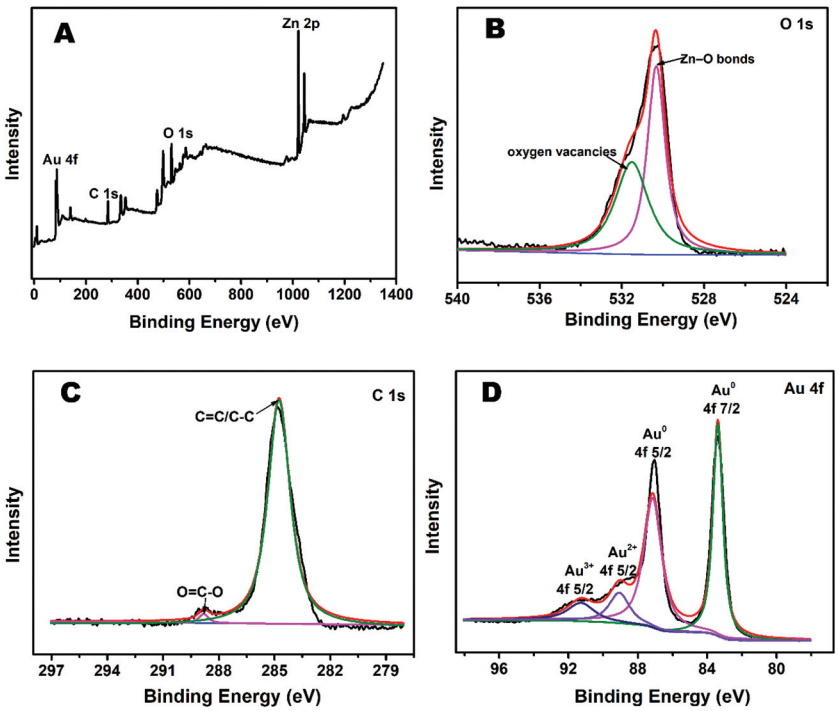

Fig. 2 (A) XPS full survey spectrum of the ZnO NRs/PTCA/Au; high resolution XPS spectra of (B) O 1s, (C) C 1s, and (D) Au 4f.

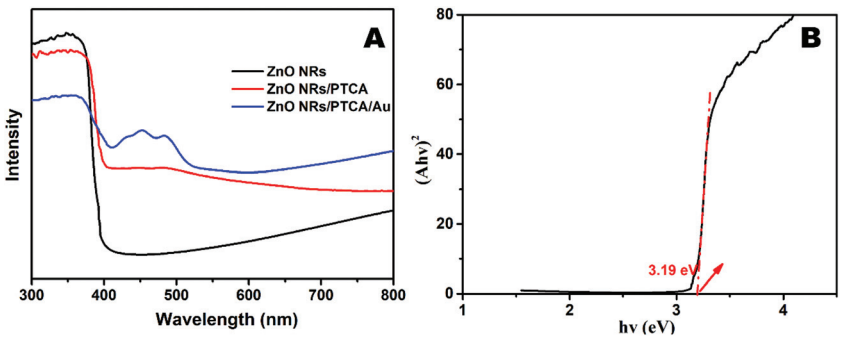

Fig. 3 (A) UV-vis diffuse reflection spectra of the as-prepared materials and (B) the $(Ah\nu)^2$ *vs.* $h\nu$ curve of the ZnO NRs.

their optical response properties. As displayed in Fig. 3A, the ZnO NRs show strong absorption mainly in the ultraviolet region. Its band gap (shown in Fig. 3B) was estimated to be 3.19 eV. Obviously, the absorption intensity of the ZnO NRs/PTCA in the visible region is enhanced after the decoration of PTCA, due to the excellent absorption properties in the visible region from the π electron transition.[35] The absorption intensity is further improved after decoration of the Au nanoparticles. The absorption range from 400 nm to 500 nm is ascribed to the SPR effect of the metal Au nanoparticles.[36] The different absorption range of plasmatic Au toward those reported in other works may be due to the different size of the Au nanoparticles and the dielectric constant of the contacted surroundings.[37,38]

Comparison of the working electrode fabrication process and detection principle

To monitor the electrical properties of the working electrode in this biosensor fabrication process, electrochemical impedance spectroscopy (EIS) analysis was carried out. In the EIS plots, electron transfer resistance (R_{et}) is the most important factor, which serves as an indicator of the interface property variation of the biosensor after different modification steps.[39] As shown in Fig. 4A, R_{et}, whose value is related to the semicircle diameter at high frequencies, decreases gradually after the decoration of PTCA (plot b) and Au (plot c). This may be due to the excellent electrical conductivity of those two materials. As expected, the R_{et} increases gradually after the

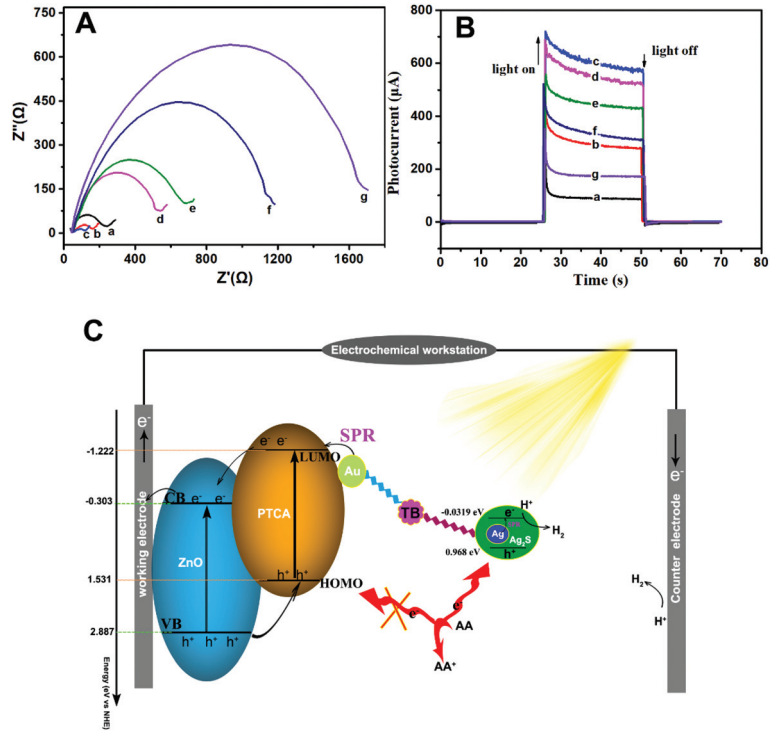

Fig. 4 (A) EIS responses and (B) photocurrent responses of Zn NRs (a), ZnO NRs/PTCA (b), ZnO NRs/PTCA/Au (c), ZnO NRs/PTCA/Au/Apt1 (d), ZnO NRs/PTCA/Au/Apt1/MCH (e), ZnO NRs/PTCA/Au/Apt1/MCH/TB (f), and ZnO NRs/PTCA/Au/Apt1/MCH/TB/Apt2-Ag@Ag_2S (g); (C) schematic illustration of the possible detection principle.

stepwise modifications of Apt1 (plot d), MCH (plot e) and TB (plot f) non-conductive materials. After the cultivation of Apt2-Ag@Ag_2S (plot g), the R_{et} increases further, resulting from the poor conductivity of Ag_2S[40] on the surface of Ag@Ag_2S and the non-conductivity of Apt2. The result indicates that the biosensor has been prepared successfully.

The above results can be also supported by the time-dependent photocurrent responses during the biosensor preparation process. As shown in Fig. 4B, thanks to the unique one dimensional vertical structure and oxygen vacancies in the ZnO NRs, the electrode shows obvious photocurrent response even under visible irradiation (plot a). Moreover, due to the broad visible light absorption and high photoelectric conversion efficiency of PTCA,[10] the photocurrent of the ZnO NRs/PTCA increases greatly (plot b). After the further decoration of plasmonic Au nanoparticles (plot c), benefiting from the synergistic effect of the ZnO NRs, PTCA and Au, the photocurrent of the electrode achieved in this work is the maximum value. With the stepwise modifications of nonconductive Apt1 (plot d), MCH (plot e) and TB (plot f), the photocurrent decreases gradually. Finally, the photocurrent decreases further after the introduction of the Apt2-Ag@Ag_2S quencher (plot g).

For the band structure information of the photoanode materials used in this work, numerous literature can be referred to.[10,24,37] In addition, Mulliken electronegativity theory[41] was used to calculate the band energy positions of the inorganic semiconductor material. The lowest unoccupied molecular orbital (LUMO) and the highest occupied molecular orbital (HOMO) of the PTCA have been determined through the density functional theory calculation. Based on the above results, the possible detection principle is illustrated in Fig. 4C. For the ZnO NRs/PTCA/Au electrode, the photogenerated electrons can be excited by absorbing photons whose energy is high enough. The excellent photoelectric conversion performance of PTCA and its rigid, coplanar π-conjugation make it easily modified on the surface of ZnO.[10] Through the well-designed inorganic/organic semiconductor composite, light absorption can be enhanced over a wider range as well as benefiting carrier separation. In addition, Au NPs possessing the surface plasmon resonance effect can enhance light absorption in the visible region and generate hot electrons.[42] The hot electrons under the electrical field amplification effect[13] can be injected directly into the LUMO of PTCA, which then flow into the conduction band (CB) of the ZnO NRs. Finally the electrons are collected at the counter electrode through the wire and participate in the reduction of H^+, thus showing as the photocurrent. At the same time, the holes are assembled in the HOMO of PTCA and neutralized by the electron donor AA. Due to the synergistic effect of the ZnO NRs, PTCA and Au, the photoelectric conversion is more efficient, benefiting the improvement of the initial photocurrent of the photoanode. After the cultivation of the TB and Ag@Ag_2S quenchers, the photocurrent is decreased greatly. The nonconductive complex including Apt1, MCH, TB and Apt2 steric

hindrance structures decrease the photocurrent due to the obstruction of the incident light and the block in the diffusion path of the electron donor AA. For the Ag@Ag_2S quencher, due to the SPR effect of Ag and the narrow band gap of Ag_2S, electrons can be excited easily and gathered at the surface of Ag_2S participating in the reduction of H^+. The holes at the valence band (VB) of Ag_2S competitively consume the electron donor AA, which can reduce the AA amount supplied to the ZnO NRs/PTCA/Au electrode. Thus, the photocurrent is reduced further. This effective "signal-off" strategy is due to the cooperative effects of the thrombin-aptamers-Ag@Ag_2S bioconjugates' steric hindrance, the quencher's light absorption competition and the competitive neutralization toward the electron donor AA.

Analytical performance, selectivity, stability and reproducibility

Under the optimized conditions (supplied in Fig. S2†), the photocurrent responses toward different concentrations of TB are shown in Fig. 5A. From 0.0001 nM to 50 nM, the curve between the photocurrent and the logarithm value of TB concentration is a good linear fit, shown in Fig. 5B. The linear detection range is wider than of the sensors based on enzymatic biofuel cells with capacitor signal amplification,[43] or the one based on a conductive supramolecular polymer hydrogel decorated electrode,[44] as well as the typical reported biosensors prepared based on electrochemical technology[45,46] and PEC sensing.[47] The regression equation is $I = -31.73\log C_{TB} + 138.71$, $R^2 = 0.99862$ and the limit of detection (LOD) was calculated to be 33 fM (S/N = 3). In Table 1, the analytical performance of this biosensor is compared with that of other reported works for thrombin detection. With respect to linear range and LOD, our biosensor is comparable to or even better than many of the reported thrombin sensors (listed in Table 1 but not limited).

Table 1 Comparison of several typical methods for thrombin detection

Analytical technique	Linear range	LOD	Ref.
Open circuit potential	0.6 pM to 0.1 nM	0.22 pM	43
Impedance spectroscopy	10 pM to 1000 nM	0.12 pM	48
DPV	1 pM to 10 nM	0.64 pM	44
DPV	5 pM to 500 nM	3 pM	49
DPV	18 pM to 10 nM	126 fM	45
SWV	5 pM to 1 nM	1.7 pM	46
PEC	0.1 pM to 8 nM	30 fM	47
PEC	50 fM to 20 pM	23 fM	50
PEC	0.1 pM to 50 nM	33 fM	This work

The selectivity of the proposed biosensor was assessed with TB and potential interferences (1 nM) including glucose, L-cys, BSA, lysozyme and K^+. As shown in Fig. 5C, only TB can cause a significant decrease in the photocurrent and the other potential interferences show negligible influences, indicating the high selectivity of this biosensor for TB detection.

The stability of this biosensor was analyzed through the photocurrent response under periodic light excitation (Fig. 5D) with the incubation of 0.1 nM TB. This biosensor exhibits a stable photoelectric property after eight cycles of intermittent irradiation, with 95.88% of the initial photocurrent left. The reproducibility of this biosensor was also studied with five independent proposed electrodes for the detection of 0.1 nM TB. The photocurrent response is shown in Fig. 6 and the relative standard deviation for the five photocurrents is calculated

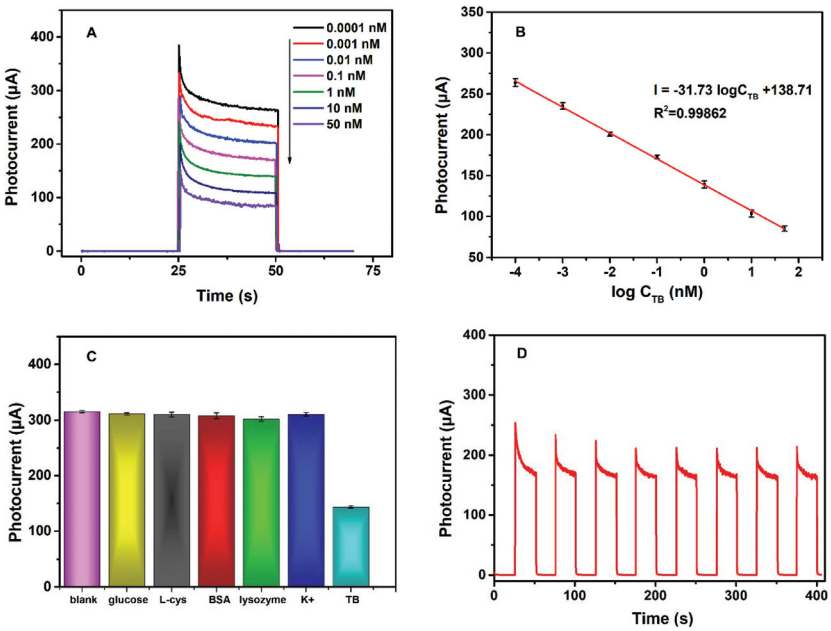

Fig. 5 (A) Photocurrent responses of the aptasensor incubated with different concentrations of TB; (B) the calibration curve of the photocurrent *versus* the logarithm of TB concentration; (C) selectivity and (D) stability of this biosensor.

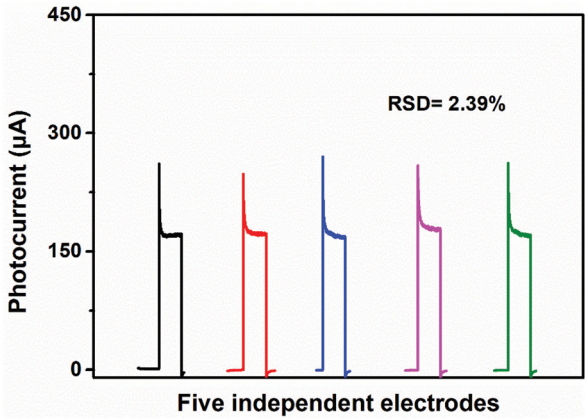

Fig. 6 Photocurrent responses of five independent proposed electrodes for 0.1 nM TB detection.

Table 2 Recovery results of the proposed aptasensor in 100-fold diluted human serum (n = 3)

Samples	Added TB (nM)	Found TB[a] (nM)	Recovery (%)	RSD (%)
1	0.01	0.0096	96	5.52
2	0.1	0.10267	102.67	4.39
3	5	5.164	103.28	2.01
4	20	20.277	101.39	3.66

[a] The average value of three measurements.

to be 2.39%, indicating the good reproducibility of this biosensor.

Real sample applicable analysis

The practical applicability of the proposed biosensor was estimated through the standard addition method. TB with different concentrations was added in 100-fold diluted human serum samples, as shown in Table 2. The recovery rate and RSD of each group are acceptable indicating that the proposed biosensor has potential application in real sample analysis.

Conclusions

In summary, an effective thrombin PEC biosensor is proposed based on the excellent photoelectric conversion efficiency of the photoactive materials and effective "signal-off" quenching strategies. Due to the synergistic effect of the one-dimensional ZnO NRs, better film-forming photosensitive organic semiconductor PTCA and the plasmonic Au nanoparticles, the photocurrent of the electrode is large enough for the initial signal of this "signal-off" design. The steric hindrance of the bioconjugates, the light absorption competition effect of Ag@Ag_2S and their electron donor AA competition neutralization with the photoanode decrease the photocurrent response, which is correlated with the target concentration. Finally, the proposed PEC biosensor exhibits acceptable performances in selectivity, stability and real analysis, benefiting from the multiple signal amplification strategies.

Conflicts of interest

The authors declare that they have no conflicts of interest.

Acknowledgements

Financial support was received from the National Natural Science Foundation of China (No. 21971152) and the Natural Science Foundation of the Shandong Province (No. ZR2018MB002).

References

1 W. Tu, Z. Wang and Z. Dai, *TrAC, Trends Anal. Chem.*, 2018, **105**, 470–483.
2 S. Z. Lv, K. Y. Zhang, L. Zhu and D. P. Tang, *Anal. Chem.*, 2020, **92**, 1470–1476.
3 M. Hu, H. Yang, Z. Li, L. Zhang, P. Zhu, M. Yan and J. Yu, *Biosens. Bioelectron.*, 2020, **147**, 111786.
4 K. Zhao, X. Q. Yan, Y. S. Gu, Z. Kang, Z. M. Bai, S. Y. Cao, Y. C. Liu, X. H. Zhang and Y. Zhang, *Small*, 2016, **12**, 245–251.
5 K. Qi, B. Cheng, J. Yu and W. Ho, *J. Alloys Compd.*, 2017, **727**, 792–820.
6 Z. Geng, X. Kong, W. Chen, H. Su, Y. Liu, F. Cai, G. Wang and J. Zeng, *Angew. Chem., Int. Ed.*, 2018, **57**, 6054–6059.
7 J. Singh and R. K. Soni, *Appl. Surf. Sci.*, 2020, **521**, 13.
8 J. Wang, Y. Xia, H. Y. Zhao, G. F. Wang, L. Xiang, J. L. Xu and S. Komarneni, *Appl. Catal., B*, 2017, **206**, 406–416.
9 H. J. Zheng, S. Zhang, X. Q. Liu, Y. M. Zhou and S. Alwarappan, *Biosens. Bioelectron.*, 2020, **162**, 10.
10 R. Zheng, M. Zhang, X. Sun, R. Chen and X. Sun, *Appl. Catal., B*, 2019, **254**, 667–676.
11 L. Yang, X. Zhong, L. Huang, H. Deng, R. Yuan and Y. Yuan, *Anal. Chim. Acta*, 2019, **1077**, 281–287.
12 W. Lv, J. Liu, Y. He and J. You, *Ceram. Int.*, 2018, **44**, 23310–23314.
13 J. Luo, Y. N. Jiang, X. Y. Guo, Y. Ying, Y. Wen, P. Lin, Y. Sun, H. F. Yang and Y. P. Wu, *Sens. Actuators, B*, 2020, **309**, 7.
14 Y. Liu, Y. S. Chang, Y. J. Hsu, B. J. Hwang and C. H. Hsueh, *Electrochim. Acta*, 2019, **321**, 8.
15 Y. X. Feng, T. Yan, T. T. Wu, N. Zhang, Q. Q. Yang, M. Sun, L. G. Yan, B. Du and Q. Wei, *Sens. Actuators, B*, 2019, **298**, 7.
16 H. Malekzad, P. S. Zangabad, H. Mirshekari, M. Karimi and M. R. Hamblin, *Nanotechnol. Rev.*, 2017, **6**, 301–329.
17 B. Zhang, H. Wang, J. Xi, F. Zhao and B. Zeng, *Electrochim. Acta*, 2020, **331**, 135350.

18 X. Y. Zhang, S. G. Liu, W. J. Zhang, X. H. Wang, L. Han, Y. Ling, N. B. Li and H. Q. Luo, *Sens. Actuators, B*, 2019, **297**, 126818.
19 L. Yang, X. Zhong, L. J. Huang, H. M. Deng, R. Yuan and Y. L. Yuan, *Anal. Chim. Acta*, 2019, **1077**, 281–287.
20 L. Meng, K. Xiao, X. Zhang, C. Du and J. Chen, *Biosens. Bioelectron.*, 2020, **150**, 111861.
21 W. C. Geng, D. L. Li, J. L. Sang, L. L. Pan, Z. L. Jiang, C. Liu and Y. J. Li, *J. Mater. Chem. B*, 2020, **8**, 10346–10352.
22 J. Feng, Y. Li, Z. Gao, H. Lv, X. Zhang, D. Fan and Q. Wei, *Biosens. Bioelectron.*, 2018, **99**, 14–20.
23 B. Liu and Z. F. Ma, *Small*, 2011, **7**, 1587–1592.
24 W. Jiang, Z. Wu, Y. Zhu, W. Tian and B. Liang, *Appl. Surf. Sci.*, 2018, **427**, 1202–1216.
25 M. Chakraborty, D. Roy, A. Biswas, R. Thangavel and G. Udayabhanu, *RSC Adv.*, 2016, **6**, 75063–75072.
26 X. Wang, S. M. Tabakman and H. Dai, *J. Am. Chem. Soc.*, 2008, **130**, 8152–8153.
27 S. Liu, H. Tao, L. Zeng, Q. Liu, Z. Xu, Q. Liu and J. L. Luo, *J. Am. Chem. Soc.*, 2017, **139**, 2160–2163.
28 M. A. Hassan, A. Waseem, M. A. Johar, I. V. Bagal, J. S. Ha and S. W. Ryu, *J. Mater. Chem. A*, 2020, **8**, 8300–8312.
29 L. He, Z. Tong, Z. Wang, M. Chen, N. Huang and W. Zhang, *J. Colloid Interface Sci.*, 2018, **509**, 448–456.
30 G. W. Zheng, J. S. Wang, H. Liu, V. Murugadoss, G. N. Zu, H. B. Che, C. Lai, H. Y. Li, T. Ding, Q. Gao and Z. H. Guo, *Nanoscale*, 2019, **11**, 18968–18994.
31 P. Li, J. Wang, H. Chen, X. Sun, J. You, S. Liu, Y. Zhang, M. Liu, X. Niu and Y. Luo, *J. Mater. Chem. A*, 2019, **7**, 12446–12450.
32 R. Narayan, J. Lim, T. Jeon, D. J. Li and S. O. Kim, *Carbon*, 2017, **119**, 555–568.
33 X. Yang, Z. Chen, D. Zhou, W. Zhao, X. Qian, Q. Yang, T. Sun and C. Shen, *Sol. Energy Mater. Sol. Cells*, 2019, **201**, 110065.
34 H. Kitagawa, N. Kojima and T. Nakajima, *J. Chem. Soc., Dalton Trans.*, 1991, 3121–3125.
35 Y. Liu, Y. D. Shi, X. Liu and H. X. Li, *Appl. Surf. Sci.*, 2017, **396**, 58–66.
36 S. W. Kang, P. R. Deshmukh, Y. Sohn and W. G. Shin, *Mater. Today Commun.*, 2019, **21**, 100675.
37 J. Zhao, B. Liu, L. Meng, S. He, R. Yuan, Y. Hou, Z. Ding, H. Lin, Z. Zhang, X. Wang and J. Long, *Appl. Catal., B*, 2019, **256**, 117823.
38 Y. C. Pu, G. M. Wang, K. D. Chang, Y. C. Ling, Y. K. Lin, B. C. Fitzmorris, C. M. Liu, X. H. Lu, Y. X. Tong, J. Z. Zhang, Y. J. Hsu and Y. Li, *Nano Lett.*, 2013, **13**, 3817–3823.
39 Q. Z. Han, R. Y. Wang, B. Xing, H. T. Chi, D. Wu and Q. Wei, *Biosens. Bioelectron.*, 2018, **106**, 7–13.
40 X. Qin, L. Geng, Q. Wang and Y. Wang, *Microchim. Acta*, 2019, **186**, 430.
41 L. Yosefi and M. Haghighi, *Appl. Catal., B*, 2018, **220**, 367–378.
42 X. Zhang, Y. Liu and Z. Kang, *ACS Appl. Mater. Interfaces*, 2014, **6**, 4480–4489.
43 Y. H. Wang, F. T. Wang, Z. W. Han, K. J. Huang, X. M. Wang, Z. H. Liu, S. Y. Wang and Y. F. Lu, *Sens. Actuators, B*, 2020, **304**, 10.
44 X. Y. Wang, F. X. Gao, Y. Y. Gong, G. T. Liu, Y. Zhang and C. F. Ding, *Talanta*, 2019, **205**, 6.
45 L. Cheng, C. Xu, H. F. Cui, F. S. Liao, N. Hong, G. Ma, J. Xiong and H. Fan, *Anal. Chim. Acta*, 2020, **1111**, 1–7.
46 J. Yang, B. Dou, R. Yuan and Y. Xiang, *Anal. Chem.*, 2017, **89**, 5138–5143.
47 Y. Zhan, J. Tang, D. Huang, L. Zou and B. Ye, *Talanta*, 2019, **198**, 302–309.
48 A. K. Yagati, A. Behrent, S. Beck, S. Rink, A. M. Goepferich, J. Min, M. H. Lee and A. J. Baeumner, *Biosens. Bioelectron.*, 2020, **164**, 10.
49 L. L. Zhang, X. Y. Zhang, P. J. Feng, Q. Han, W. Liu, Y. Lu, C. X. Song and F. Y. Li, *Anal. Chem.*, 2020, **92**, 7419–7424.
50 C. Li, Y. Cai, M. Pang, X. Zhou, X. Luo and Z. Xiao, *Biosens. Bioelectron.*, 2020, **147**, 111779.